This is the author's version of a work that was submitted/accepted for publication in the following source:

Effective cell-centred time-domain Maxwell's equations numerical solvers for the purpose of microwave heating

V.Vegh[†]

School of Mathematical Sciences

Centre in Statistical Science and Industrial Mathematics

Queensland University of Technology

GPO BOX 2434

Brisbane Q4001 Australia

mailto: v.vegh@qut.edu.au

I. W. Turner

School of Mathematical Sciences

Centre in Statistical Science and Industrial Mathematics

Queensland University of Technology

GPO BOX 2434

Brisbane Q4001 Australia

mailto: i.turner@fsc.qut.edu.au

H. Zhao

Centre in Magnetic Resonance

Level 2, Gehrmann Laboratories

University of Queensland,

Brisbane Q4072 Australia

mailto: bob.zhao@cmr.uq.edu.au

[†] corresponding author

Abstract

This research work analyses techniques for implementing a cell-centred finite-volume time-domain computational methodology for the purpose of microwave heating. Various state-of-the-art spatial and temporal discretisation methods employed to solve Maxwell's equations on multi-dimensional structured grid networks are investigated, and the dispersive and dissipative errors inherent in those techniques examined. Both staggered and unstaggered grid approaches are considered. Upwind schemes using a Riemann solver and intensity vector splitting are studied and evaluated. Staggered and unstaggered Leapfrog and Runge-Kutta time integration methods are analysed in terms of phase and amplitude error to identify which method is the most accurate and efficient for simulating microwave heating processes. The implementation and migration of typical electromagnetic boundary conditions from staggered in space to cell-centred approaches also is deliberated. In particular, an existing Perfectly Matched Layer absorbing boundary methodology is adapted to formulate a new cell-centred boundary implementation for the ccFV-TD solvers. Finally for microwave heating purposes, a comparison of analytical and numerical results for standard case studies in rectangular waveguides allows the accuracy of the developed methods to be assessed.

1. Introduction

Over the years, numerous computational models have been investigated and developed for the solution of Maxwell's equations for a variety of important applications in Science and Engineering [1-4]. Typically, researchers implement solution methodologies that simulate instantaneous electromagnetic fields, and these are used to obtain the steady-state electromagnetic wave phenomena inside a microwave heating apparatus.

The scope of this research work focuses on the use of cell-centred time-domain finite-volume (ccFV-TD) solvers for investigating electromagnetic field behaviour during microwave heating processes. For domestic and industrial microwave heating applications, the time-averaged electric and magnetic fields have to be computed. From the computed time-averaged fields the power can be obtained easily, and hence, the microwave power distribution can be coupled with the forced heat equation to obtain the temperature distribution inside the dielectric medium.

In this paper, numerous cell-centred time-domain schemes are presented and assessed in terms of computational speed, phase and amplitude error, in order to identify the most accurate and efficient method that can be used to obtain the time-averaged electric field distribution inside the load in a waveguide. The time-averaged fields are computed for various case studies, and are compared to the results obtained using the classical finite-difference time-domain (FD-TD) [5] and the analytic solutions where possible. The computation of the power and subsequently the determination of the heat distribution inside the medium are left to future research by the authors.

Historically, both the integral and point forms of the governing Maxwell's equations have been approximated in Computational Electromagnetics (CEM). The ccFV-TD methods discussed here are formulated from a discrete volume-surface representation of the governing equations. When developing finite-volume or finite-difference stencils to locate the electromagnetic unknowns within a discrete cell, the approximations to the components of the electromagnetic fields are stored at different spatial locations. For example, FD-TD uses

the Yee lattice to locate the components of the unknowns around a cell. The electric and magnetic fields are staggered also in time in order to stabilise the explicit time marching scheme.

Cell-centred schemes store all of the electromagnetic fields at the same spatial location, which is normally at the centre of the finite-volume cell. Given that the spatial locations of the electric and magnetic field components are located at the same point, cell-centred schemes are much easier to manage, develop and implement in comparison with their staggered counterparts. By the nature of the staggering of the unknowns in the FD-TD method, the inherent errors are reduced and this location in time and space of the electric and magnetic field components establishes a highly accurate scheme for structured grids. Unfortunately due to this staggering, the FD-TD scheme is difficult to implement on unstructured grids, and in this case cell-centred schemes are more viable. Nevertheless, rigorous consideration needs to take place to achieve sufficient accuracy in the cell-centred schemes. Despite the fact that for each cell the unknowns are positioned at the same spatial location, it is still possible to stagger the electric and magnetic field components in time. For cell-centred schemes this can stabilise the time marching of the numerical solver. It is possible also that higher order approximations in both time and space have to be considered to obtain a more accurate ccFV-TD scheme.

In the last decade, techniques from Computational Fluid Dynamics (CFD) have been adapted to CEM [4, 6, 7] with reasonable success. In this work, the uses of intensity vector splitting (IVS) and Riemann solvers (RS) are analysed, and mathematical formulations are given. Methods that employ techniques from CFD are known to be dissipative by nature. Munz et al [8] discuss a finite-volume solver for the Maxwell's equations in curvilinear non-orthogonal coordinates without the use of dimensional splitting. The local wave propagation between adjacent grid cells is determined by the solution of Riemann problems. A thorough analysis of the characteristic methods used to determine the required solution is given in [4] and the reader is referred there for the finer details.

The characteristic theory [4] requires the flux to be split into + and – states at a cell interface, then a number of different numerical approximations are applied to determine these states. In this work, the schemes used to approximate the states are presented in a way that can easily be generalised to a completely unstructured mesh framework. However, in an attempt to gauge the accuracy and efficiency of the schemes investigated, it was decided to restrict the study here only to a structured mesh domain based on hexahedra, since the FD-TD method performs accurately on such grids and can be used for comparison. The migration of the cell-centred finite-volume method to an unstructured case will be the subject of future research.

Note that when these CFD type schemes are used to dampen any oscillatory behaviour due to spatial discretisation errors caused by the cell-centred strategy, it becomes necessary to employ higher order time integration techniques to resolve the differential system in time. Here 3rd and 4th order Runge-Kutta (RK3, RK4) methods are implemented on the cell-centred approaches to analyse their performance. However, the schemes that do not contain the damping term are discretised in time using second order Leapfrog time marching schemes that are staggered and unstaggered in time. Also, the schemes that utilise RK3 and RK4 time integrations with damping are implemented without the inclusion of the damping term, so that the effect of the term from the CFD methodology can be analysed for CEM applications.

In this paper, the solutions of typical waveguide problems are presented for two distinct case studies. The first concerns an empty waveguide study and the second a loaded waveguide study. The same numerical solvers are implemented in both cases. Initially, a detailed description of the mathematical formulation is provided for the time domain cell-centred in space methods, and typical boundary condition implementation for the conducting walls, input plane, material interface and a new cell-centred absorbing boundary layer is deliberated. In the scattered region of the waveguide, an existing Perfectly Matched Layer

(PML) methodology [9] is reformulated and complemented for cell-centred schemes. As a subsequence, this new PML formulation is adapted to the cell-centred finite-volume schemes to absorb any reflected impinging waves in the scattered field region of the waveguide.

Primarily, the empty waveguide study allows the performance of the different Maxwell's equation time-domain solvers to be analysed under free space conditions. Depending on the spatial and temporal discretisation methods utilised, the schemes exhibit both dispersive and dissipative numerical errors. Dissipative errors cause the loss of wave amplitude, while dispersive errors affect the wave propagation speed. These errors are cumulative in nature and their analyses are provided in the form of phase and loss or gain in amplitude. The time-averaged electric fields inside an empty waveguide are investigated. The computed fields are compared to both the FD-TD and exact solutions. It is observed that the second order accurate in space and time cell-centred methods are competitive in terms of accuracy and efficiency when compared to the FD-TD solver.

For the next case study, the waveguide is analysed when loaded with a dielectric material. A number of simulations for a short-circuited rear end loaded waveguide are presented. The simulation results are then compared to the analytic and FD-TD solutions. A loaded multi-mode waveguide is analysed also, and the results are compared to the FD-TD method. It is shown that cell-centred schemes can be implemented in a straightforward manner to resolve the time averaged electric fields inside a waveguide structure, and capture the analytic and FD-TD solutions more than adequately. The outcomes indicate that cell-centred schemes can be used with confidence for simulating the microwave power inside a load within a microwave apparatus.

This paper is organised as follows. In the next section, the mathematical formulation for discretising Maxwell's equations using a finite-volume approach is presented, highlighting the different cell-centred schemes. Followed by a detailed discussion of the EM boundary condition implementation. Thereafter, the results for the different waveguide case studies

6

are presented and comparisons between the various methods are provided via a number of graphical illustrations that elucidate the dissipative and dispersive nature of the different schemes. A table of amplitude and phase errors is provided also to highlight the evident differences between the methods. Finally, the main conclusions of this work are summarised.

2. Mathematical Formulations

For the purpose of numerical simulation using a finite-volume methodology, the point form of the Maxwell's equations:

$$\nabla \times \mathbf{E} = -\frac{\partial \mathbf{B}}{\partial t}, \qquad \nabla \times \mathbf{H} = \frac{\partial \mathbf{D}}{\partial t} + \mathbf{J}, \tag{1}$$

$$\mathbf{B} = \mu_0 \mathbf{H}, \quad \mathbf{D} = \varepsilon \mathbf{E}, \quad \mathbf{J} = \sigma \mathbf{E}, \quad \varepsilon = \varepsilon_0 \varepsilon', \quad \sigma = \omega \varepsilon_0 \varepsilon'',$$

must be recast into a discrete volumetric form by integrating over a discrete finite-volume cell to obtain:

$$\iiint_V \nabla \times \mathbf{E} \, \partial V = -\iiint_V \frac{\partial \mathbf{B}}{\partial t} \, \partial V, \qquad \iiint_V \nabla \times \mathbf{H} \, \partial V = \iiint_V \frac{\partial \mathbf{D}}{\partial t} \, \partial V + \iiint_V \mathbf{J} \, \partial V. \tag{2}$$

Unlike approximating an integral formulation based on the Stokes' theorem [3, 10], the Divergence theorem together with the relevant vector identities are applied to (2), to obtain the following surface-volume representation:

$$\iint_S \mathbf{n} \times \mathbf{E} \, \partial S = -\iiint_V \frac{\partial \mathbf{B}}{\partial t} \, \partial V, \qquad \iint_S \mathbf{n} \times \mathbf{H} \, \partial S = \iiint_V \frac{\partial \mathbf{D}}{\partial t} \, \partial V + \iiint_V \mathbf{J} \, \partial V. \tag{3}$$

The continuous eq. (3) is then approximated by the discrete form as follows:

$$\frac{\partial \mathbf{B}_p}{\partial t} = -\frac{1}{\Delta V} \sum_{F \in \zeta_p} \mathbf{n} \times \mathbf{E}_F \, \Delta S_F, \qquad \frac{\partial \mathbf{D}_p}{\partial t} = \frac{1}{\Delta V} \sum_{F \in \zeta_p} \mathbf{n} \times \mathbf{H}_F \, \Delta S_F - \mathbf{J}_p. \tag{4}$$

where, $\mathbf{n}$ is the unit outward normal through a face of a particular cell (see Fig. 1). In the equations, ζ_p is the set of faces that constitute the pth cell in the computational domain. ΔS_F and ΔV are the surface area of a particular face in ζ_p and the volume of the pth cell, respectively. If $\mathbf{E}_F$ and $\mathbf{H}_F$ represent the values at the midpoint of the face, the above

7

discrete surface integral approximation is second order in space. When all of the cells that constitute the mesh that describe the solution domain are visited, a system of ordinary differential equations (ODEs) results. Numerous methods are applied to resolve this ODE system.

Time discretisation can introduce either dispersion or dissipation errors (see [4]). Numerous techniques are utilised to resolve (4) into time discrete form. In [11] a number of approaches similar to the FD-TD technique have been investigated. For a function φ, (5a-b) represent the staggered (SLF) and unstaggered (ULF) leapfrog discretisations respectively. The SLF and ULF schemes are both $O(\Delta t^2)$:

$$\frac{\partial \varphi}{\partial t}^n = \frac{\varphi^{n+\frac{1}{2}} - \varphi^{n-\frac{1}{2}}}{\Delta t}, \tag{5a}$$

$$\frac{\partial \varphi}{\partial t}^n = \frac{\varphi^{n+1} - \varphi^{n-1}}{2\Delta t}. \tag{5b}$$

Methods using the discretisations in (5) have been used in the past to numerically solve for the electromagnetic fields governed by the Maxwell's equations. Using (5a), (4) can be written in discrete form as:

$$\mathbf{H}_p^{n+\frac{1}{2}} = \mathbf{H}_p^{n-\frac{1}{2}} - \frac{\Delta t}{\mu_0 \Delta V} \sum_{F \in \zeta_p} \mathbf{n} \times (\mathbf{E}_F)^n \, \Delta S_F, \tag{6a}$$

$$\mathbf{E}_p^{n+1} = \frac{2\varepsilon - \sigma \Delta t}{2\varepsilon + \sigma \Delta t} \mathbf{E}_p^n + \frac{2\Delta t}{(2\varepsilon + \sigma \Delta t)\Delta V} \sum_{F \in \zeta_p} \mathbf{n} \times (\mathbf{H}_F)^{n+\frac{1}{2}} \, \Delta S_F. \tag{6b}$$

Similarly, (4) for the ULF discretisation becomes:

$$\mathbf{H}_p^{n+1} = \mathbf{H}_p^{n-1} - \frac{2\Delta t}{\mu_0 \Delta V} \sum_{F \in \zeta_p} \mathbf{n} \times (\mathbf{E}_F)^n \, \Delta S_F, \tag{7a}$$

$$\mathbf{E}_p^{n+1} = \frac{\varepsilon - \sigma \Delta t}{\varepsilon + \sigma \Delta t} \mathbf{E}_p^{n-1} + \frac{2\Delta t}{(\varepsilon + \sigma \Delta t)\Delta V} \sum_{F \in \zeta_p} \mathbf{n} \times (\mathbf{H}_F)^n \, \Delta S_F. \tag{7b}$$

Eqs. (6) and (7) require the approximation to the electric and magnetic fields on the cell faces. It is possible to postulate a number of interpolation and extrapolation schemes to approximate these cell face unknowns. On structured grids, the simplest way to approximate

the unknowns at a cell face is by averaging the values about a particular face. Such a technique yields a second order in space and time approximation to (6) and (7). These particular finite-volume methods will be referred to as SLF (6), staggered in time and unstaggered in space, and ULF (7), unstaggered in time and space Leapfrog discretisations.

At the pth cell in (4), intensity vector splitting (IVS) [4] is applied to replace the $\mathbf{n} \times \mathbf{E}_F$ and the $\mathbf{n} \times \mathbf{H}_F$ terms. The idea of IVS is to include an extra term in the flux facial expression to dampen any numerical oscillations, and to capture any discontinuities (such as shocks and contact surfaces in CFD) in the solution. Intensity vector splitting originally from CFD, is based on the + and − characteristics to approximate the unknowns at a cell face. Eq. (8) shows the general form at a cell face F of the IVS result:

$$\mathbf{n} \times \mathbf{E}_F = \tfrac{1}{2}\mathbf{n} \times (\mathbf{E}_F^+ + \mathbf{E}_F^-) + \tfrac{1}{2}\mathbf{n} \times \left\{ [\mu c]^+ \mathbf{n} \times \mathbf{H}_F^+ - [\mu c]^- \mathbf{n} \times \mathbf{H}_F^- \right\}, \tag{8a}$$

$$\mathbf{n} \times \mathbf{H}_F = \tfrac{1}{2}\mathbf{n} \times (\mathbf{H}_F^+ + \mathbf{H}_F^-) - \tfrac{1}{2}\mathbf{n} \times \left\{ [\varepsilon c]^+ \mathbf{n} \times \mathbf{E}_F^+ - [\varepsilon c]^- \mathbf{n} \times \mathbf{E}_F^- \right\}, \tag{8b}$$

where, the wave speed is given by $c = 1/\sqrt{\mu\varepsilon}$. Riemann invariants can also be applied to determine the left and right states at a cell face. The Riemann solver (RS) was introduced by Shankar [6]:

$$\mathbf{n} \times \mathbf{E}_F = \mathbf{n} \times \left\{ \frac{(\varepsilon c)_R}{((\varepsilon c)_R + (\varepsilon c)_L)} \mathbf{E}_R + \frac{(\varepsilon c)_L}{(\varepsilon c)_R + (\varepsilon c)_L} \mathbf{E}_L \right\} + \mathbf{n} \times \frac{1}{(\varepsilon c)_R + (\varepsilon c)_L} \mathbf{n} \times \left\{ \mathbf{H}_R - \mathbf{H}_L \right\}, \tag{9a}$$

$$\mathbf{n} \times \mathbf{H}_F = \mathbf{n} \times \left\{ \frac{(\mu c)_R}{((\mu c)_R + (\mu c)_L)} \mathbf{H}_R + \frac{(\mu c)_L}{(\mu c)_R + (\mu c)_L} \mathbf{H}_L \right\} - \mathbf{n} \times \frac{1}{(\mu c)_R + (\mu c)_L} \mathbf{n} \times \left\{ \mathbf{E}_R - \mathbf{E}_L \right\}. \tag{9b}$$

In free space, it can be shown that RS reduces to IVS. It is evident from IVS and RS that the + and − characteristics, or the right (R) and left (L) states must be approximated for each cell face. Note that IVS cannot be implemented with (6), since the values for the magnetic and electric fields are required at different time levels. Numerical experimentation has shown that IVS and RS with (7) incurs large errors due to the time discretisation [4]. Therefore, higher order time stepping methods are to be implemented. The following 3rd order Runge-Kutta (RK3) method is used for the numerical schemes discussed above:

$$\varphi^{n+\frac{1}{3}} = \varphi^n + \frac{\Delta t}{3} \frac{\partial \varphi}{\partial t}^n , \quad \varphi^{n+\frac{2}{3}} = \varphi^n + \frac{2\Delta t}{3} \frac{\partial \varphi}{\partial t}^{n+\frac{1}{3}} ,$$

$$\varphi^{n+1} = \varphi^{n} + \frac{\Delta t}{4}\left(3\frac{\partial\varphi}{\partial t}^{n+\frac{2}{3}} + \frac{\partial\varphi}{\partial t}^{n}\right). \tag{10a}$$

A 4th order Runge-Kutta (RK4) method is implemented also, and is formulated below:

$$\hat{\varphi}^{n+\frac{1}{2}} = \varphi^{n} + \frac{\Delta t}{2}\frac{\partial\varphi}{\partial t}^{n}, \quad \widetilde{\varphi}^{n+\frac{1}{2}} = \varphi^{n} + \frac{\Delta t}{2}\frac{\partial\hat{\varphi}}{\partial t}^{n+\frac{1}{2}},$$

$$\overline{\varphi}^{n+1} = \varphi^{n} + \Delta t\frac{\partial\widetilde{\varphi}}{\partial t}^{n+\frac{1}{2}}, \quad \varphi^{n+1} = \varphi^{n} + \frac{\Delta t}{6}\left(\frac{\partial\varphi}{\partial t}^{n} + 2\frac{\partial\hat{\varphi}}{\partial t}^{n+\frac{1}{2}} + 2\frac{\partial\widetilde{\varphi}}{\partial t}^{n+\frac{1}{2}} + \frac{\partial\overline{\varphi}}{\partial t}^{n+1}\right). \tag{10b}$$

Substituting either of the IVS or RS results leads to numerical techniques referred to as RK3-IVS (RK3-RS) and RK4-IVS (RK4-RS), respectively. Note that (4) can be solved without the inclusion of damping, and this idea is pursued later in this section. Furthermore, other Runge-Kutta methods can be used to resolve the system of ODEs from above. These are not discussed here, but will be analysed in another paper where the schemes highlighted here will be applied on unstructured grids.
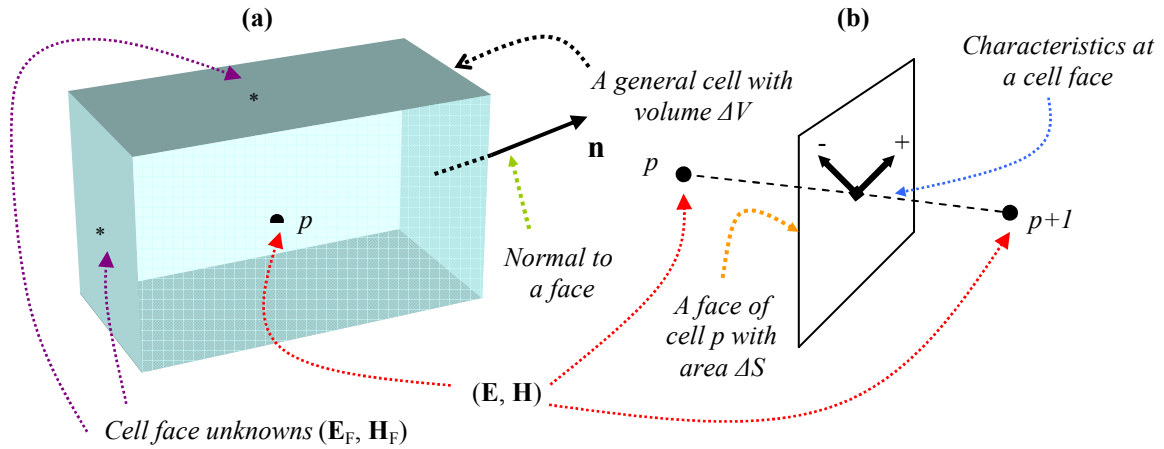

Figure 1. *A general cell within the computational domain; (a) 3D cell with unknown locations; (b) The characteristics at a face of a particular cell.*

For simplicity, Fig. (1) illustrates a typical cell within a 3D-structured computational domain. As depicted, the + and − characteristics for IVS, and the right and left states for RS are required on a particular cell face and different strategies can be derived to approximate the values at the cell face joining any two adjacent cells. For example, an unknown ξ can be approximated using the 0th order substitution:

$$\xi^-_{p+\frac{1}{2}} = \xi_p, \quad \xi^+_{p+\frac{1}{2}} = \xi_{p+1}. \tag{11}$$

Imposing the 0th order approximation in RK3/RK4-IVS/RS leads to two first order in space and 3rd order in time approximations known as RK3-1-IVS and RK3-1-RS, and two first order in space and 4th order in time approximations identified as RK4-1-IVS and RK4-1-IVS. For a structured uniform mesh, it is possible to derive a general one-sided linear extrapolation model that is 2nd order in space:

$$\xi^-_{p+\frac{1}{2}} = \tfrac{1}{2}(3\xi_p - \xi_{p-1}), \quad \xi^+_{p+\frac{1}{2}} = \tfrac{1}{2}(3\xi_{p+1} - \xi_{p+2}). \tag{12}$$

As for the 0th order extrapolations, using (12) the equivalent 3rd and 4th order in time and 2nd order in space numerical schemes are called RK3-2L-IVS/RS and RK4-2L-IVS/RS, respectively. It is important to note that (12) is developed for uniform in x, y and z coordinate structured grids. Such extrapolations are complicated to implement on unstructured meshes, and are demonstrated only to assess the errors between the different schemes.

Given discrete data points, it is also possible to find least squares gradient approximations at cell centres [12]. Eq. (13) expresses a truncated representation of the Taylor series:

$$\delta\mathbf{r} \cdot \nabla\xi(\mathbf{r}) \approx \xi(\mathbf{r} + \delta\mathbf{r}) - \xi(\mathbf{r}). \tag{13}$$

The above system can be cast into matrix form as $\mathbf{A} \cdot \nabla\xi_p = \mathbf{d}$. The gradient that minimises $\|\mathbf{A} \cdot \nabla\xi_p - \mathbf{d}\|^2$ with respect to the inner product on $\mathbb{R}^k$ can be obtained by solving the normal equations. The value of k equals the number of neighbouring nodes utilised to obtain the gradient at the pth cell. Although approximations for the gradients that utilise the hypercube (k =26) have been investigated, in this paper the gradients were constructed using only adjacent cells of ζ_p (ie. k =6). Hence by evaluating (13), the gradients of the fields are used to approximate the characteristics at the cell faces. Accordingly, (14) provides a 2nd order approximation for the + and – fields, or the right and left states and the subsequent methods are classified as RK3-2G-IVS, RK4-2G-IVS, RK3-2G-RS and RK4-2G-RS, depending on the time integration and whether intensity vector splitting or the Riemann solver is applied:

$$\xi_{p+\frac{1}{2}}^{-} = \xi_{p} + \boldsymbol{\delta}' \cdot \nabla \xi_{p}, \quad \xi_{p+\frac{1}{2}}^{+} = \xi_{p+1} + \boldsymbol{\delta}'' \cdot \nabla \xi_{p+1}. \tag{14}$$

In (14), $\boldsymbol{\delta}'$ and $\boldsymbol{\delta}''$ are the vectors from the nodes (p) to $(p+\frac{1}{2})$ and (p+1) to $(p+\frac{1}{2})$, respectively (see Fig. (1)). Also, the gradients can be approximated using the Gauss-Green reconstruction [12]:

$$\nabla \xi_{p} \approx \frac{1}{V_{p}} \sum_{F \in \varsigma_{p}} \mathbf{n} \xi_{F},$$

where, V_{p} is the volume of the pth cell and $\mathbf{n}$ is the unit outward normal to face F. On structured grids, when the Gauss-Green reconstruction is used to approximate the values of characteristics at the cell faces in RK3/RK4-IVS and RK3/RK4-RS, the resulting equations reduce to that obtained by the least squares gradients (13).

The RK3/RK4-2L-IVS/RS and RK3/RK4-2G-IVS/RS methods can also be applied without flux splitting (ie. IVS and RS). These techniques will be referred to as the RK3/RK4-2L and RK3/RK4-2G schemes, which are the linear extrapolation and the spatial gradient approximations without intensity vector splitting and Riemann invariants, respectively.

3. Implementation of Boundary Conditions

In this section, the perfectly conducting wall, incident field, material interface and absorbing boundary conditions are treated. On a perfectly conducting wall in a microwave heating apparatus, the following conditions need to be satisfied [13]:

$$\mathbf{n} \times \mathbf{E} = \mathbf{0}, \quad \mathbf{n} \cdot \mathbf{H} = 0. \tag{15}$$

Eq. (15) makes the assumption that there is no loss through the perfect conductor. If there is some loss associated with the conducting wall boundaries, then impedance conditions should be used instead of (15). Fig. (2) shows the characteristics in the proximity of a perfectly conducting wall. It can be seen from the figure, that at the wall, only one of the characteristics exists. For the numerical treatment of the conducting wall boundary condition, a spurious external layer surrounding the whole computational domain is introduced, as shown in Fig (2). The numerically simulated boundary information of (16) is

constructed in a way that ensures the conditions of (15) are enforced at the cell faces that lie on the conducting wall.
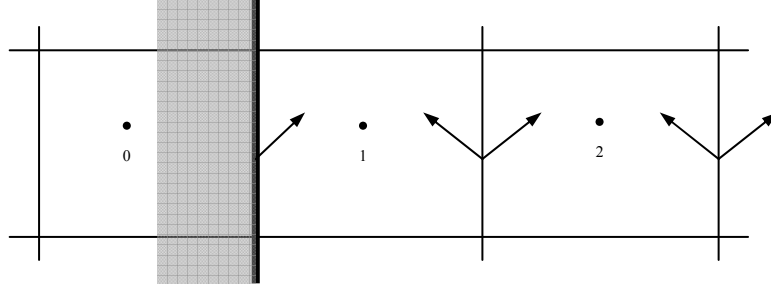

Figure 2. Boundary condition treatment at a Perfectly Conducting Wall.

Hence, the following spurious fields are constructed:

$$(\mathbf{E}_0^*)_t = -(\mathbf{E}_1)_t, \quad (\mathbf{E}_0^*)_n = (\mathbf{E}_1)_n, \tag{16a}$$

$$(\mathbf{H}_0^*)_t = (\mathbf{H}_1)_t, \quad (\mathbf{H}_0^*)_n = -(\mathbf{H}_1)_n. \tag{16b}$$

where, * represents the fields introduced externally to the original domain to satisfy the boundary conditions (15), when the standard discrete in space Maxwell's equations (4) are used on the perfectly conducting boundary. For the spurious field evaluations, t and n are the tangential and normal components of the electric and magnetic fields, respectively. The conditions (16) are used in the ULF, SLF, RK3/RK4-2G and RK3/RK4-1-IVS/RS simulations. For the RK3/RK4-2L with and without IVS/RS, a secondary layer is introduced for the extrapolations. For the second order linear extrapolation models, (17) has to be implemented together with (16):

$$(\mathbf{E}_{-1}^*)_t = -(\mathbf{E}_2)_t, \quad (\mathbf{E}_{-1}^*)_n = (\mathbf{E}_2)_n, \tag{17a}$$

$$(\mathbf{H}_{-1}^*)_t = (\mathbf{H}_2)_t, \quad (\mathbf{H}_{-1}^*)_n = -(\mathbf{H}_2)_n. \tag{17b}$$

Techniques such as RK3/RK4-2G-IVS/RS that employ the gradients for the approximations at the cell faces require (16) together with the following spurious field conditions to be satisfied:

$$(\nabla \mathbf{E}_0^*)_t = -(\nabla \mathbf{E}_1)_t, \quad (\nabla \mathbf{E}_0^*)_n = (\nabla \mathbf{E}_1)_n, \tag{18a}$$

$$(\nabla \mathbf{H}_0^*)_t = (\nabla \mathbf{H}_1)_t, \quad (\nabla \mathbf{H}_0^*)_n = -(\nabla \mathbf{H}_1)_n. \tag{18b}$$

Eq. (18) is necessary in the boundary information evaluation for schemes that obtain the facial values according to (14), since it satisfies (15) at a cell face that lies on a perfectly conducting wall boundary. Given the above formulations, the boundary conditions on a perfectly conducting wall are guaranteed in (4) according to (15). Similarly, other discrete conditions can be developed that provide continuity of the tangential magnetic fields and ensure zero tangential electric fields at a perfectly conducting wall, but these are not discussed here.
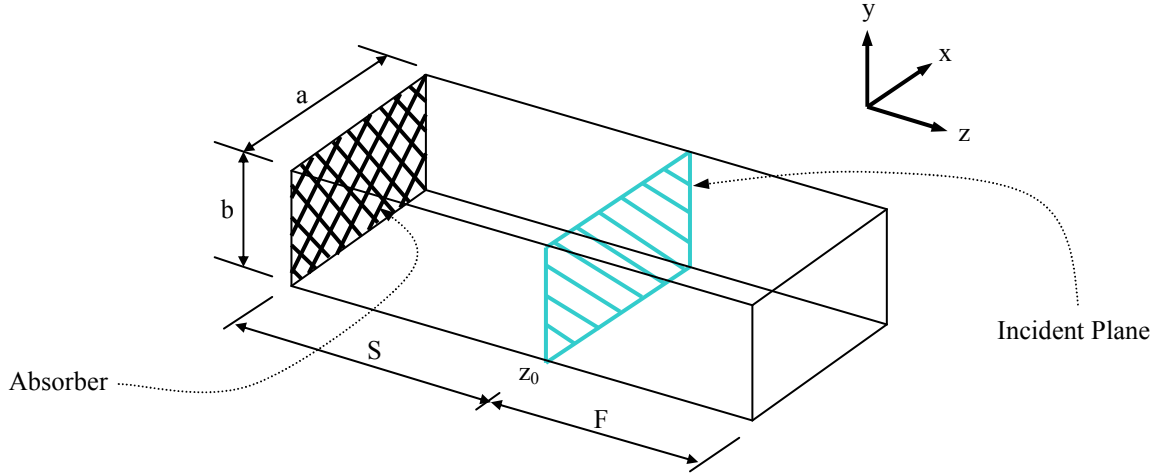

Figure 3. A waveguide with incident and absorbing boundary conditions.

A classical waveguide is demonstrated in Fig (3). In the figure, S and F represent the scattered and full field regions inside a waveguide, respectively. Typically, a fictitious dielectric is introduced inside the scattered region to absorb any reflected backward travelling waves.

Fig. (4) illustrates the situation arising at the incident plane, where the electromagnetic fields are excited. It is assumed that z_0 represents the location where the incident field is applied. T, S and I are the total, scattered and incident field classifications, respectively. In the full field region of the waveguide the total fields have to be computed, while in the scattered field region only the scattered fields are computed. Across an input plane this is achieved by adding the incident field to the scattered field in F, and subtracting the incident field from the total field in S (see Fig. (4)). This is sufficient to propagate a wave in the z-coordinate direction. In this paper, a continuous TE_{10} incident field has been implemented for the input

14

boundary condition. At the input plane, the scattered and full fields were computed according to the following expressions:

$$E_y^I = E_0 \sin(\frac{\pi x}{a})\cos(\omega t - \beta_0 z_0) , \tag{19a}$$

$$H_x^I = -\frac{\beta_0}{\omega\mu_0} E_0 \sin(\frac{\pi x}{a})\cos(\omega t - \beta_0 z_0) , \tag{19b}$$

$$H_z^I = -\frac{\pi}{\omega\mu_0 a} E_0 \cos(\frac{\pi x}{a})\sin(\omega t - \beta_0 z_0) , \tag{19c}$$

$$E_0 = 2\sqrt{\frac{P_0}{ab\varepsilon_0}} , \quad \beta_0 = \sqrt{\omega^2 \mu_0 \varepsilon_0 - \left(\frac{\pi}{a}\right)^2} .$$

In (19), P_0 is the average input power, and a and b are the dimensions as labelled in Fig.3. Fig. (3) also illustrates an absorbing boundary layer. There are two main types of absorbers, the MUR type absorbing boundary condition [14] and the Perfectly Matched Layer (PML) [9, 15, 16]. The 1st order MUR type boundary condition is given as:

$$\left[\left(\frac{\partial}{\partial z} - \frac{1}{c}\frac{\partial}{\partial t}\right)\varphi\right]_{z=0} = 0 . \tag{20}$$

where, *c* is the wavefront speed inside the waveguide. In the past, this boundary condition has been widely implemented in the FD-TD scheme. In this paper, it is employed in the FD-TD and ULF numerical simulations. While MUR type boundary conditions are obtained from splitting the wave equation into positive and negative travelling waves, the PML boundary condition is based on matching the impedance of the absorbing medium to the impedance of free-space. There are a number of different types of PML boundary conditions, all of which are based on the following augmented Maxwell's equations:

$$\frac{\partial \mathbf{B}}{\partial t} + \mathbf{J}^* = -\nabla \times \mathbf{E}, \qquad \frac{\partial \mathbf{D}}{\partial t} + \mathbf{J} = \nabla \times \mathbf{H} , \tag{21a}$$

where,

$$\mathbf{J}^* = \sigma^* \mathbf{H}, \qquad \sigma^* = \frac{\mu_0}{\varepsilon_0}\sigma . \tag{21b}$$

The Berenger type PML [16] absorber splits some of the components of the fields inside the absorption layer. Such a methodology increases memory usage and is also more computationally exhaustive, as opposed to more recent PML absorbers that do not split the fields [9]. If (21b) is satisfied for the absorbing boundary condition, then the impedance of the PML equals that of free-space, and no reflections occur. Now, (1) can be replaced by (21) in the discretisation, and new discrete in space equations can be obtained for the simulation of Maxwell's equations within the absorbing material:

$$\frac{\partial \mathbf{B}}{\partial t} = -\frac{1}{\Delta V} \sum_{F} \mathbf{n} \times \mathbf{E}_{F} \, \Delta S_{F} - \mathbf{J}_{p}^{*}, \qquad \frac{\partial \mathbf{D}}{\partial t} = \frac{1}{\Delta V} \sum_{F} \mathbf{n} \times \mathbf{H}_{F} \, \Delta S_{F} - \mathbf{J}_{p}. \qquad (22)$$

For the schemes discussed in this paper, (22) is implemented using a new cell-centred adaptation of the Petropoulos PML boundary condition [9]. For the absorbing boundary region, only the normal components need to be treated in (22). The tangential components are still governed by (4). Consequently, (22) can be discretised and formulated with and without IVS/RS.

In the theory by Petropoulos, an extra term in the evaluations of the normal components inside the PML region has to be approximated. This extra term consists of an integral from time zero to the current time step of the numerical solver. The approximation of this time integral has to be carefully treated, so that the time stepping of the numerical solver is consistent with the computation of the time integral. Hence, the step size in the numerical integration must coincide with the time marching of the discrete Maxwell's equations solver (22). The update for the numerical integration is therefore a sum, which is accumulated according to the time resolution of (22). The PML formulation for the SLF technique is similar to that discussed in [9], the only difference being in the location of the spatial unknowns. The SLF implementation for the normal component at a point p of (for example) the magnetic field is formulated from (22) as follows:

$$\Delta V \left(\frac{\partial \mathbf{B}}{\partial t} \right)_{p} = -\sum_{F \in \zeta_{P}} \left(\mathbf{n} \times \mathbf{E}_{F} \right)_{p} \Delta S_{F} - \frac{\sigma^{*}}{\mu_{0}} \int_{0}^{t} \iint_{S} \left(\mathbf{n} \times \mathbf{E}_{F} \right)_{p} \partial S dt , \qquad (23a)$$

16

$$\Delta V \left(\frac{\partial \mathbf{B}}{\partial t} \right)_p = -\sum_{F \in \zeta_P} \left(\mathbf{n} \times \mathbf{E}_F \right)_p \Delta S_F - I \text{, where} \tag{23b}$$

$$I = \frac{\sigma^*}{\mu_0} \int_0^t \sum_{F \in \zeta_P} \left(\mathbf{n} \times \mathbf{E}_F \right)_p \Delta S_F \, dt = \frac{\sigma^*}{\mu_0} \int_0^{n \Delta t} \sum_{F \in \zeta_P} \left(\mathbf{n} \times \mathbf{E}_F \right)_p \Delta S_F \, d\tau . \tag{23c}$$

In (23), the integral has to be approximated using numerical integration techniques. For the SLF method, the components of the electric and magnetic fields are located at the nth and the $(n+\frac{1}{2})^{th}$ time levels. The numerical integration that approximates (23c) has to ensure that the scheme updates the integral at every ½ time steps. For this reason, the numerical integration is performed using a two increment trapezoidal rule. Given that at time zero the electric and magnetic fields are zero, then (23c) can be approximated as:

$$I = \frac{\sigma^*}{\mu_0} \Delta t \sum_{m=0}^{n-1} \left[\sum_{F \in \zeta_P} \left(\mathbf{n} \times \mathbf{E}_F \right)_p^m \Delta S_F \right] + \frac{\sigma^*}{2\mu_0} \Delta t \sum_{F \in \zeta_P} \left(\mathbf{n} \times \mathbf{E}_F \right)_p^n \Delta S_F . \tag{24}$$

The following expression is obtained when (24) is substituted back into (23b) and resolved using SLF (5a):

$$\mathbf{H}_p^{n+\frac{1}{2}} = \mathbf{H}_p^{n-\frac{1}{2}} - \left(\frac{2\mu_0 \Delta t + \sigma^* \Delta t^2}{2\mu_0^2 \Delta V} \right) \sum_{F \in \zeta_P} \left(\mathbf{n} \times \mathbf{E}_F \right)_p^n \Delta S_F - \frac{\sigma^* \Delta t^2}{\mu_0^2 \Delta V} \mathbf{F}_p^{n-1} , \tag{25a}$$

$$\mathbf{F}_p^n = \mathbf{F}_p^{n-1} + \sum_{F \in \zeta_P} \left(\mathbf{n} \times \mathbf{E}_F \right)_p^n \Delta S_F . \tag{25b}$$

Similarly, the normal component of the electric field within the PML region is defined as:

$$\mathbf{E}_p^{n+1} = \mathbf{E}_p^n + \left(\frac{2\varepsilon \Delta t + \sigma \Delta t^2}{2\varepsilon^2 \Delta V} \right) \sum_{F \in \zeta_p} \left(\mathbf{n} \times \mathbf{H}_F \right)_p^{n+\frac{1}{2}} + \frac{\sigma \Delta t^2}{\varepsilon^2 \Delta V} \mathbf{G}_p^{n-\frac{1}{2}} , \tag{26a}$$

$$\mathbf{G}_p^{n+\frac{1}{2}} = \mathbf{G}_p^{n-\frac{1}{2}} + \sum_{F \in \zeta_p} \left(\mathbf{n} \times \mathbf{H}_F \right)_p^{n+\frac{1}{2}} \Delta S_F . \tag{26b}$$

The following equations are generated for the 3rd order ODE solver, when the above theory is reformulated to cater for the RK time integrations:

$$\left(\frac{\partial \mathbf{H}_p}{\partial t} \right)^n = -\left(\frac{\sigma^* \Delta t + 6\mu_0}{6\mu_0^2 \Delta V} \right) \sum_{F \in \zeta_p} \left(\mathbf{n} \times \mathbf{E}_F \right)^n \Delta S_F - \frac{\sigma^* \Delta t}{3\mu_0^2 \Delta V} \mathbf{F}_p^{n-1} , \tag{27a}$$

$$\left(\frac{\partial \mathbf{E}_p}{\partial t} \right)^n = \left(\frac{\sigma \Delta t + 6\varepsilon_0}{6\varepsilon_0^2 \Delta V} \right) \sum_{F \in \zeta_p} \left(\mathbf{n} \times \mathbf{H}_F \right)^n \Delta S_F + \frac{\sigma \Delta t}{3\varepsilon_0^2 \Delta V} \mathbf{G}_p^{n-1} , \tag{27b}$$

where,

$$\mathbf{F}_p^n = \mathbf{F}_p^{n-1} + \sum_{F \in \varsigma_p} (\mathbf{n} \times \mathbf{E}_F)^{n-\frac{2}{3}} \Delta S_F + \sum_{F \in \varsigma_p} (\mathbf{n} \times \mathbf{E}_F)^{n-\frac{1}{3}} \Delta S_F + \sum_{F \in \varsigma_p} (\mathbf{n} \times \mathbf{E}_F)^n \Delta S_F , \qquad (27c)$$

$$\mathbf{G}_p^n = \mathbf{G}_p^{n-1} + \sum_{F \in \varsigma_p} (\mathbf{n} \times \mathbf{H}_F)^{n-\frac{2}{3}} \Delta S_F + \sum_{F \in \varsigma_p} (\mathbf{n} \times \mathbf{H}_F)^{n-\frac{1}{3}} \Delta S_F + \sum_{F \in \varsigma_p} (\mathbf{n} \times \mathbf{H}_F)^n \Delta S_F . \qquad (27d)$$

For the 4th order Runge-Kutta method, the normal equations inside the PML are treated by the following discretisations:

$$\left(\frac{\partial \mathbf{H}_p}{\partial t} \right)^n = -\left(\frac{\sigma^* \Delta t + 4\mu_0}{4\mu_0^2 \Delta V} \right) \sum_{F \in \zeta_p} (\mathbf{n} \times \mathbf{E}_F)^n \, \Delta S_F - \frac{\sigma^* \Delta t}{2\mu_0^2 \Delta V} \mathbf{F}_p^{n-1} , \qquad (28a)$$

$$\left(\frac{\partial \mathbf{E}_p}{\partial t} \right)^n = \left(\frac{\sigma \Delta t + 4\varepsilon_0}{4\varepsilon_0^2 \Delta V} \right) \sum_{F \in \zeta_p} (\mathbf{n} \times \mathbf{H}_F)^n \, \Delta S_F + \frac{\sigma \Delta t}{2\varepsilon_0^2 \Delta V} \mathbf{G}_p^{n-1} , \qquad (28b)$$

where,

$$\mathbf{F}_p^n = \mathbf{F}_p^{n-1} + \sum_{F \in \varsigma_p} (\mathbf{n} \times \mathbf{E}_F)^{n-\frac{1}{2}} \Delta S_F + \sum_{F \in \varsigma_p} (\mathbf{n} \times \mathbf{E}_F)^n \Delta S_F , \qquad (28c)$$

$$\mathbf{G}_p^n = \mathbf{G}_p^{n-1} + \sum_{F \in \varsigma_p} (\mathbf{n} \times \mathbf{H}_F)^{n-\frac{1}{2}} \Delta S_F + \sum_{F \in \varsigma_p} (\mathbf{n} \times \mathbf{H}_F)^n \Delta S_F . \qquad (28d)$$

For the different time levels of the RK3 solver, (27c-d) are updated at the nth, (n+1/3)th and (n+2/3)th time levels, while for the RK4 solver, (28c-d) are determined at the nth and the (n+1/2)th time levels. For the Petropoulos approximation within the PML region, the **F** and **G** terms are obtained using a trapezoidal integration. The number of steps taken to update the equations of (27c-d) and (28c-d) depends on the number of time levels for which the time integration is considered (see eq. (10)).
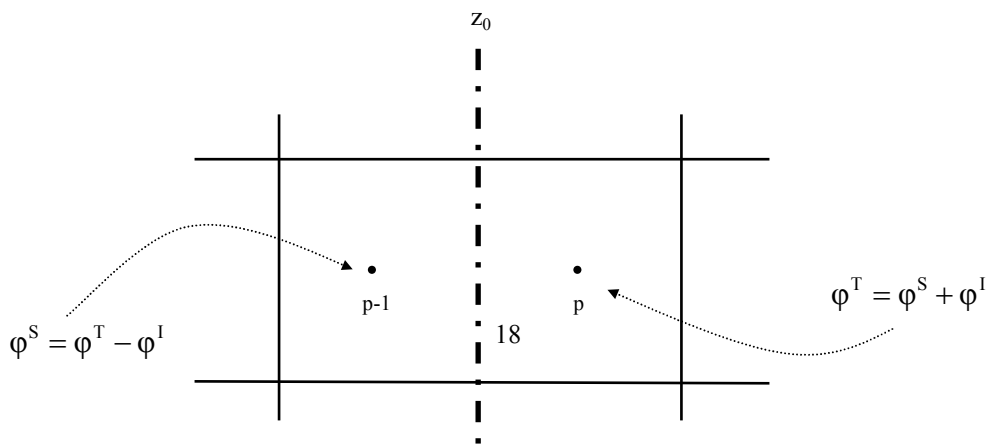

$\varphi^S = \varphi^T - \varphi^I$

p-1

18

p

$\varphi^T = \varphi^S + \varphi^I$

z$_0$

Fig. (5) depicts an interface between free-space and a material inside a waveguide. To treat and propagate an electromagnetic wave across an interface in Fig. (5), the following conditions have to be satisfied across a material boundary:

$$\mathbf{n} \times (\mathbf{E}_2 - \mathbf{E}_1) = \mathbf{0} , \tag{29a}$$

$$\mathbf{n} \cdot (\varepsilon_2 \mathbf{E}_2 - \varepsilon_1 \mathbf{E}_1) = 0 , \tag{29b}$$

$$\mathbf{n} \times (\mathbf{H}_2 - \mathbf{H}_1) = \mathbf{0} , \tag{29c}$$

$$\mathbf{n} \cdot (\mathbf{H}_2 - \mathbf{H}_1) = 0 . \tag{29d}$$

On Cartesian grids, (29a) and (29c) imply that the tangential fields across a material interface have to be equal. Eq. (29) assumes that the permeability of the different materials across and interface is constant. In the past, schemes that utilise IVS/RS were developed to capture any discontinuities across such interfaces.
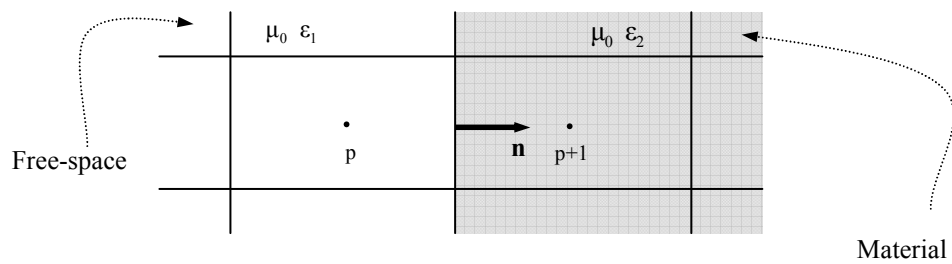

Figure 5. A free-space and material interface boundary.

It is well known that discontinuities can occur in the derivatives of the electromagnetic fields across a material interface. According to [17], plane wave assumptions can be made to capture the solution more accurately across a material interface in the FD-TD scheme. The plane wave assumption at an interface proposed by Zhao is adapted for particular ccFV-TD schemes, and the theory is demonstrated via a simplified Taylor expansion:

$$\xi_{p+1} = \xi_{p+\frac{1}{2}}^{+} + \delta x \left(\frac{\partial \xi}{\partial x}\right)_{p+\frac{1}{2}}^{+} + O(\delta x^{2}), \quad \xi_{p} = \xi_{p+\frac{1}{2}}^{-} - \delta x \left(\frac{\partial \xi}{\partial x}\right)_{p+\frac{1}{2}}^{-} + O(\delta x^{2}), \qquad (30)$$

where, δx on a structured uniform grid is the distance from any cell-centre to any face. Assuming that the waves near an interface behave in a plane wave manner, the following condition has to be satisfied at a material interface [17]:

$$\frac{1}{\beta_2}\left(\frac{\partial \xi}{\partial x}\right)_{p+\frac{1}{2}}^{+} = \frac{1}{\beta_1}\left(\frac{\partial \xi}{\partial x}\right)_{p+\frac{1}{2}}^{-}. \qquad (31)$$

The (p+½) spatial location can be thought of as the material interface, and then by substituting (31) into (30), the following approximation at a dielectric interface is obtained:

$$\xi_{p+\frac{1}{2}} = \frac{\beta_2}{\beta_1 + \beta_2}\xi_p + \frac{\beta_1}{\beta_1 + \beta_2}\xi_{p+1} + O(\delta x^{2}), \qquad (32)$$

$$\beta_i \propto \sqrt{\varepsilon_i'\left(1 + \sqrt{1 + \left(\frac{\varepsilon_i''}{\varepsilon_i'}\right)^2}\right)}, \quad i = 1, 2.$$

Generally, β_1 is associated with the properties of free space and β_2 is associated with the properties of the dielectric material. Eq. (32) can be shown to be a second order approximation to the facial values at the interface. This technique is applied in the SLF, RK3-2G and RK4-2G approximations to propagate the numerical estimates across a dielectric boundary. Note that if $\beta_1 = \beta_2$, as is the case for free space cell faces, (32) is equivalent to averaging ξ_p and ξ_{P+1} to obtain the required facial value. Consequently, (32) can be employed everywhere within the ccFV-TD solver to estimate values at the cell faces.

4. Results and Discussion

A waveguide of dimension 0.1m x 0.05m x 0.4m was excited using a TE_{10} wave, with an average input power of $P_0 = 1W$. The ccFV-TD solvers established in the previous sections were used to simulate the electromagnetic wave phenomenon for fourteen periods, and fields for the last two periods were averaged and illustrated graphically. The incident field has been smoothed according to the following Gaussian pulse to remove any rapid changes in the introduction of the TE_{10} fields [17]:

20

$$gauss(t) = \begin{cases} e^{-(\frac{t}{T}-3)^2} & t \le 3T \\ 1 & t > 3T \end{cases}. \qquad (33)$$

In (33), T represents the wave period inside the waveguide. In all of the studies, the time stepping of the numerical solver was constrained by the following relationship:

$$\Delta t = \frac{0.9}{c_{max} \sqrt{\frac{1}{\delta x^2} + \frac{1}{\delta y^2} + \frac{1}{\delta z^2}}}. \qquad (34)$$

where, c_{max} is the maximum wave speed expected in the waveguide, and δx, δy and δz are the minimum mesh dimensions in the x, y and z coordinate directions. The domain of the waveguide was discretised into 96 000 (40 x 20 x 120) Cartesian cells. In Tab. (1) the components together with their acronyms for each numerical solver investigated throughout this section are summarised.

Acronym	Definition
FD-TD	Finite-Difference Time-Domain Method with beta correction at an interface and MUR type absorbing layer
ULF	Unstaggered in time and centred in space Leapfrog method with MUR type absorber
SLF	Staggered in time and centred in space Leapfrog method with Petropolous type PML absorbing layer
Beta	Any method that utilises beta correction at an interface between free-space and material
1	One sided 1st order in space extrapolation to approximate cell face unknowns
2L	One sided 2nd order in space linear extrapolation is used in the numerical solver
2G	The gradients are calculated and used via the Taylor series to approximate the values at a cell face
RK3	Time marching was performed using the 3rd order Runge Kutta method and Petropolous type absorbing layer is used to absorb the waves in the scattered region of the waveguide
RK4	The ODEs in time were approximated via the 4th order Runge Kutta scheme and Pertropolous type absorber is used for the absorbing boundary condition
RS	The Riemann Solver equations were used to replace the terms at a cell face
IVS	Intensity-Vector Splitting was used to dampen any oscillatory behaviour in the numerical solutions
Int or Interface	Case of IVS, where IVS was applied only at a material interface
Not Int or Not Interface	IVS was applied everywhere inside the computational domain, except at a material interface
Mat or Material	IVS was applied inside the domain of the material, and not anywhere else

Table 1. The definitions of the numerous numerical schemes that are exhibited.

For the empty waveguide study, the instantaneous electromagnetic fields were monitored over a number of periods. The fields were compared to the exact solution. From the comparison, the phase difference was approximated using a least squares technique. Given the exact solution, it was assumed that the computed fields had some phase error

associated with them.   Using this assumption, the exact solution was formulated using a

phase angle relation:

$$E_C = E_0 \cos(\omega t + \beta z + \varphi),$$ (37)

where, E_C is the computed field value at a particular point in space and after some number

of time steps. E_0 is the exact electric field amplitude, and φ is the phase error. β and z are

dependent on the microwave heating apparatus.   At a point in space, the values were

computed for a period of the microwave, and the phase error was approximated using a least

squares technique.   Once the phase angle between the computed and analytic solutions was

established, the amplitude error evident in the schemes was estimated using the standard

norms.   The results for the different schemes are outlined in Tab. (2).   It should be noted that

due to the implementation of the smoothing of (33), the results obtained from the simulations

performed much better than expected.   At the input plane if no smoothing was applied, then

the FD-TD method clearly outperformed the ccFV-TD schemes.   The schemes when

implemented without smoothing had a tendency to oscillate around the analytic solution.   The

reason for this is that the electromagnetic waves without (33) are not introduced into the

apparatus in a smooth manner, but rather in an instantaneous way.   The time averaged

solutions in the figures were obtained according to the expression:

$$E_{av} = \frac{1}{N} \sum_{i=1}^{N} \left(\left| E_x \right| + \left| E_y \right| + \left| E_z \right| \right).$$ (35)

For a TE_{10} empty waveguide, the E_x and E_z fields are zero, therefore (35) reduces to a time

averaged E_y field:

$$E_{y\_av} = \frac{1}{N} \sum_{i=1}^{N} \left| E_y \right|.$$ (36)

In free-space, the RS scheme reduces to the IVS scheme, and hence in this case study,

references will be made only to the IVS simulations.

It is important to note that during the numerical simulations, not all of the E_x, E_z and H_y

fields were zero, as expected for an empty TE_{10} waveguide.   It was found that the schemes

22

that utilise the IVS strategy produced a slight error of 0.1% in these fields. This error was thought to be a side effect of the implementation of damping, and regarded as negligible in comparison with the E_y field. In fact, the use of (35) instead of (36) to compute the time averaged fields revealed no significant change in the graphs. From Tab. (2), it can be seen that the methods that utilise IVS tend to have larger amplitude errors. This is due to the fact that the CFD type algorithms dampen any oscillatory behaviour, and through this process the amplitude of the wave is somewhat reduced also. It is observed that RK4-1-IVS incurs large dissipation errors in the amplitude of the wave (see Fig. (6d)). This is due to the lower order spatial discretisation utilised. It is seen from Figs. (7c-d) that the introduction of IVS reduces the amplitude of the wave. It is not evident in the full field region of the guide, but can be clearly seen in the scattered field region, when compared to RK4-2G. There appears to be no obvious difference between RK3 and RK4 time integration techniques for the empty waveguide study. This is observed in Tab. (2) and Figs. (7a-b).

SCHEME	AMPLITUDE ERROR			PHASE ERROR		CPU TIME
	1-Norm	2-Norm	inf-Norn	Mean	Variance	Normalised
FD-TD	0.0741637	0.0694287	0.0672323	0.6818206	0.0008836	0.0666667
SLF	0.0681339	0.0643379	0.0643557	0.6784976	0.0007899	0.0797814
RK4-2L	0.0672170	0.0620855	0.0550679	0.7249154	0.0008259	0.6464480
RK3-2G	0.0647705	0.0624504	0.0660729	0.4855492	0.0007476	0.4557377
RK4-2G	0.0647643	0.0624570	0.0662543	0.4855753	0.0007509	0.6289617
RK3-1-IVS	0.0892745	0.1024925	0.1375204	0.5302919	0.0007921	0.6420765
RK4-1-IVS	0.0892570	0.1024751	0.1374970	0.5303072	0.0007920	0.8715847
RK3-2G-IVS	0.0879133	0.1015108	0.1274249	0.6106417	0.0006905	0.7404371
RK4-2G-IVS	0.0879282	0.1015241	0.1274409	0.6106659	0.0006905	1.0000000

Table 2. *Analysis of the different ccFV-TD methods. Instantaneous amplitude and phase errors are*
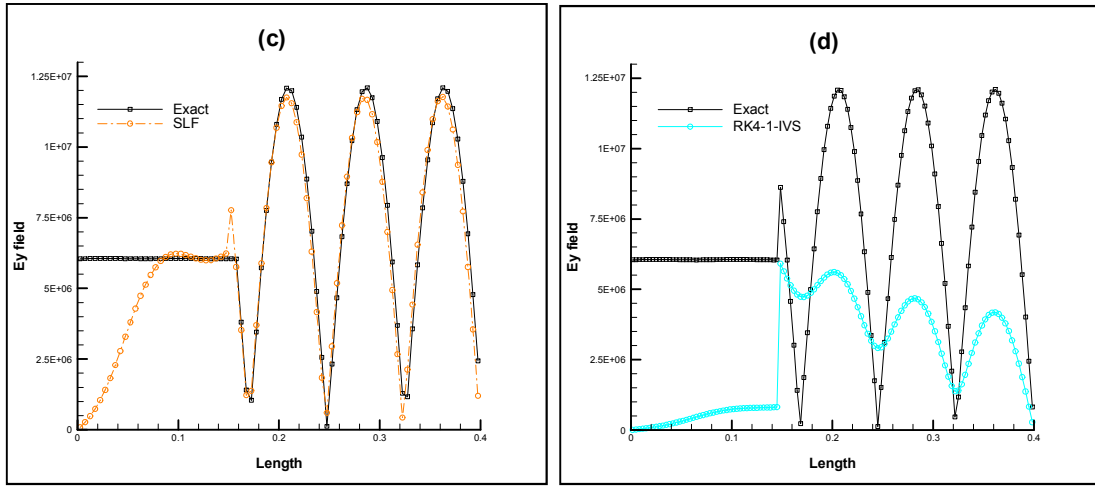
illustrated for an empty waveguide.
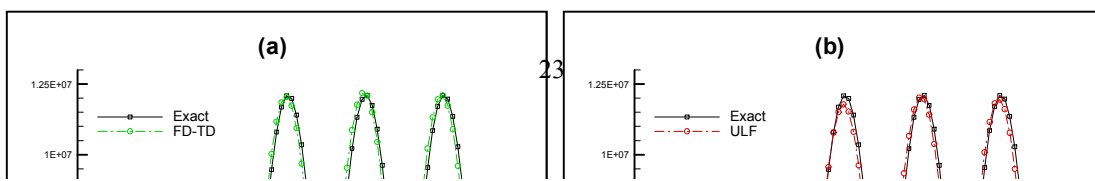
Figure 6. *A fourteen period time averaged continuous TE10 wave inside a waveguide;*

(a)FD-TD; (b) ULF; (c) SLF; (d) RK4-1-IVS.

The phase errors in Tab. (2) are of less significance for microwave heating purposes. Phase errors are related to the speed at which the wave travels along the waveguide. The observed differences in phase are of the order of nanoseconds in time, and hence, when numerically computing electromagnetic waves for the purpose of microwave heating, nanosecond shifts in the solutions are of little importance. Although, the phase analysis does provide a good estimate of the accuracy of the different ccFV-TD schemes. It should be noted that the values in Tab. (2) were calculated after two periods. Numerical error can be cumulative in nature, and hence, the clear distinctions between the observed and the calculated values (eg. RK4-1-IVS in Tab. (2) and Fig. (6d)). From the table it can be observed that the RK type methods without IVS can capture the solution better than any other scheme highlighted here. Though, it must be noted that this study does not reflect the situation when there is a material present.
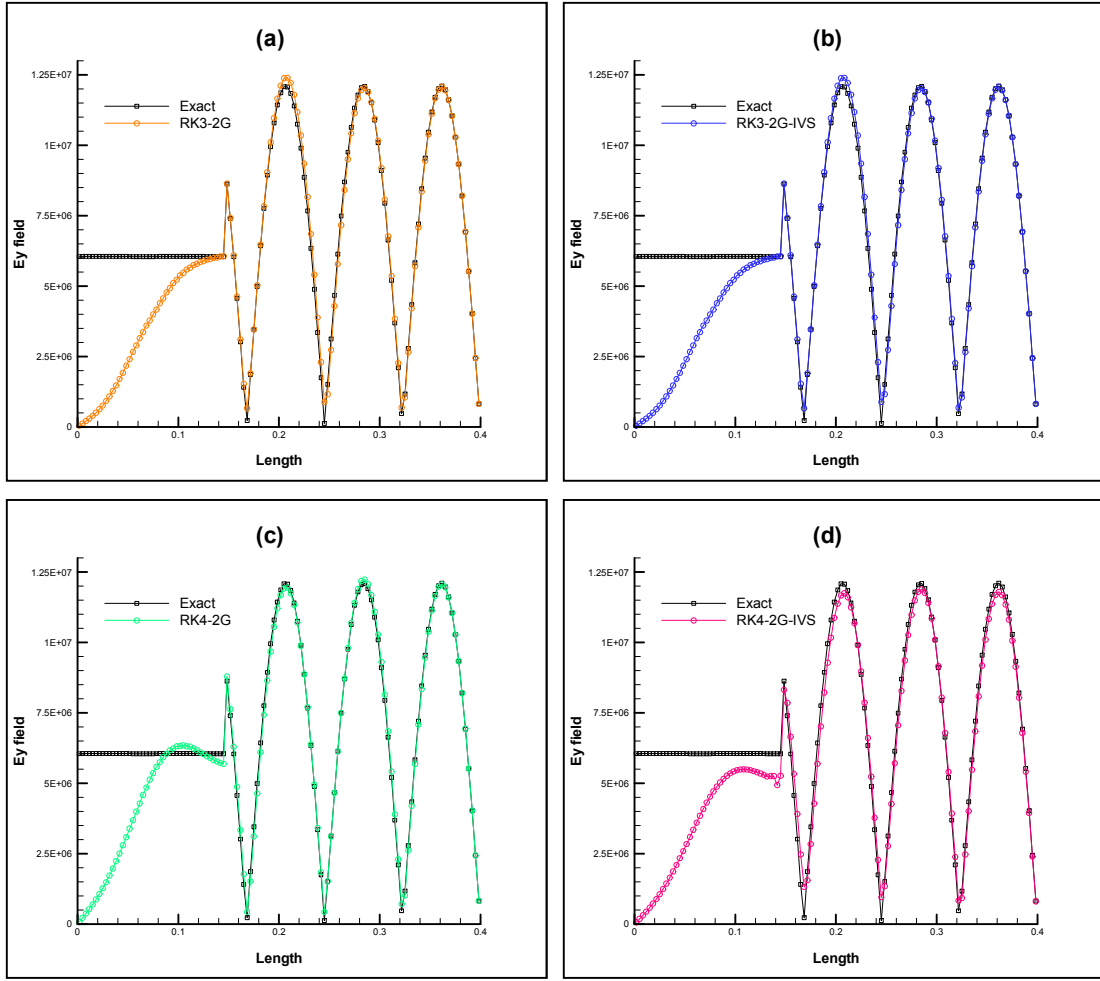
24

Figure 7. *A fourteen period time averaged continuous TE10 wave inside a waveguide;*
(a) RK3-2G; (b) RK3-2G-IVS; (c) RK4-2G; (d) RK4-2G-IVS.

The Leapfrog time integration numerical simulations illustrated in Figs. (6a-c) are observed to be performing well, although, it can be shown that the ULF scheme (see Fig. (6b)) is conditionally unstable [4]. Since the ULF scheme was found to unstable when an object was present, it will not be discussed hereafter. In Figs. (6a) and (6c) the only difference is the location of the spatial unknowns. It is clear that in an empty waveguide the SLF method is more than comparable to the FD-TD scheme.
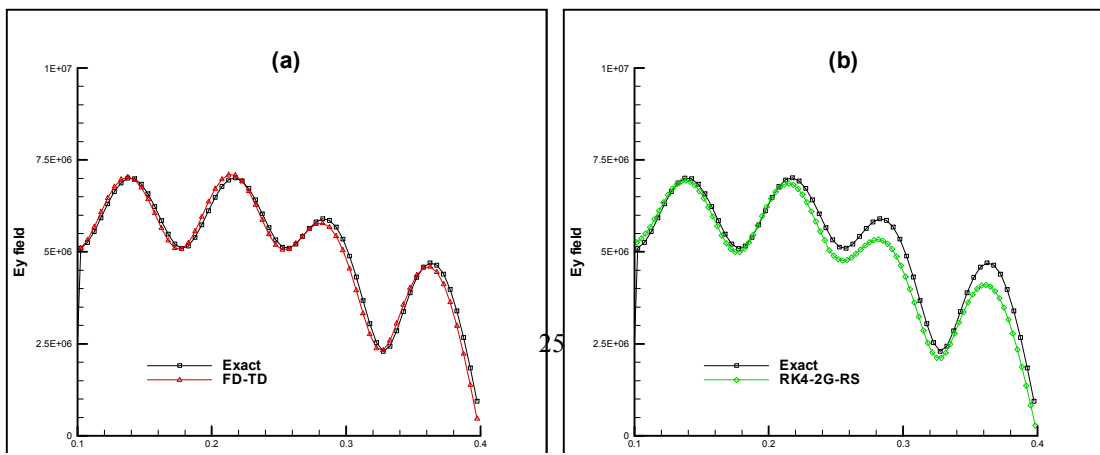
Figure 8. *A fully loaded waveguide with* $\varepsilon_r = 1 - 0.2j$; *(a) FD-TD; (b) RK4-2G-RS; (c) SLF;*

(d) SLF-beta; (e) RK3-2G; (f) RK3-2G-IVS.

Results for the empty waveguide have been tabulated. For the other studies conducted hereafter, results will be demonstrated graphically. This is because for microwave heating purposes, the requirement is for time averaged solutions. It is not possible to determine the phase error from values that have been averaged over a number of periods. It should also be noted that in Tab. (1) the CPU time has been normalised against the biggest. This is because the computations were performed on a workstation, with limited amounts of memory. It is expected that given more memory (RAM), the performance of the schemes would dramatically increase. The large differences observed between the low and high order

time integration methods is largely due to the fact that the storage requirements of the solver exceeded the available memory, and the computer was forced into using some virtual memory for the computations. Future research will investigate unstructured methods for the solution of microwave heating problems. These will be implemented on high performance computers with large amounts of memory, and hence, more comparable results with regards to CPU time will be demonstrated.

Figs. (8-11) depict the results generated for a waveguide that is fully loaded from $z = 0.25$ metres to $z = 0.4$ metres. In Figs. (8-9) the permittivity of the load is $\varepsilon_r = 1 - 0.2j$, while in Figs. (10-11) the dielectric property of the material is $\varepsilon_r = 2 - 0.5j$. In the second case, the absorptivity of the material is much larger, and due to the material's properties, more waves should reflect at the dielectric interface. The electric fields have been computed according to (36). In all of the studies, the FD-TD scheme has been implemented with the beta correction (32) at an interface.

Fig. (8d) shows the result for the SLF method under the plane wave assumption (28), and Fig. (9b) shows the beta correction when RK4 time integration is applied. In these figures, it can be seen that for the first dielectric property investigated, the plane wave assumption is of little significance (see Figs. (8c-d) and (9a-b)).

It can be seen in Figs. (8-9) that when using the beta correction at an interface, the results are comparable to the related schemes that do not utilise the beta correction. However, the absorptivity of the material is increased, and the reflections due to the phase changes become more evident, it is clear that by applying the beta correction in the SLF and RK4-2G schemes, the results are smoother (see Figs. (10c-d) and (11a-b)).
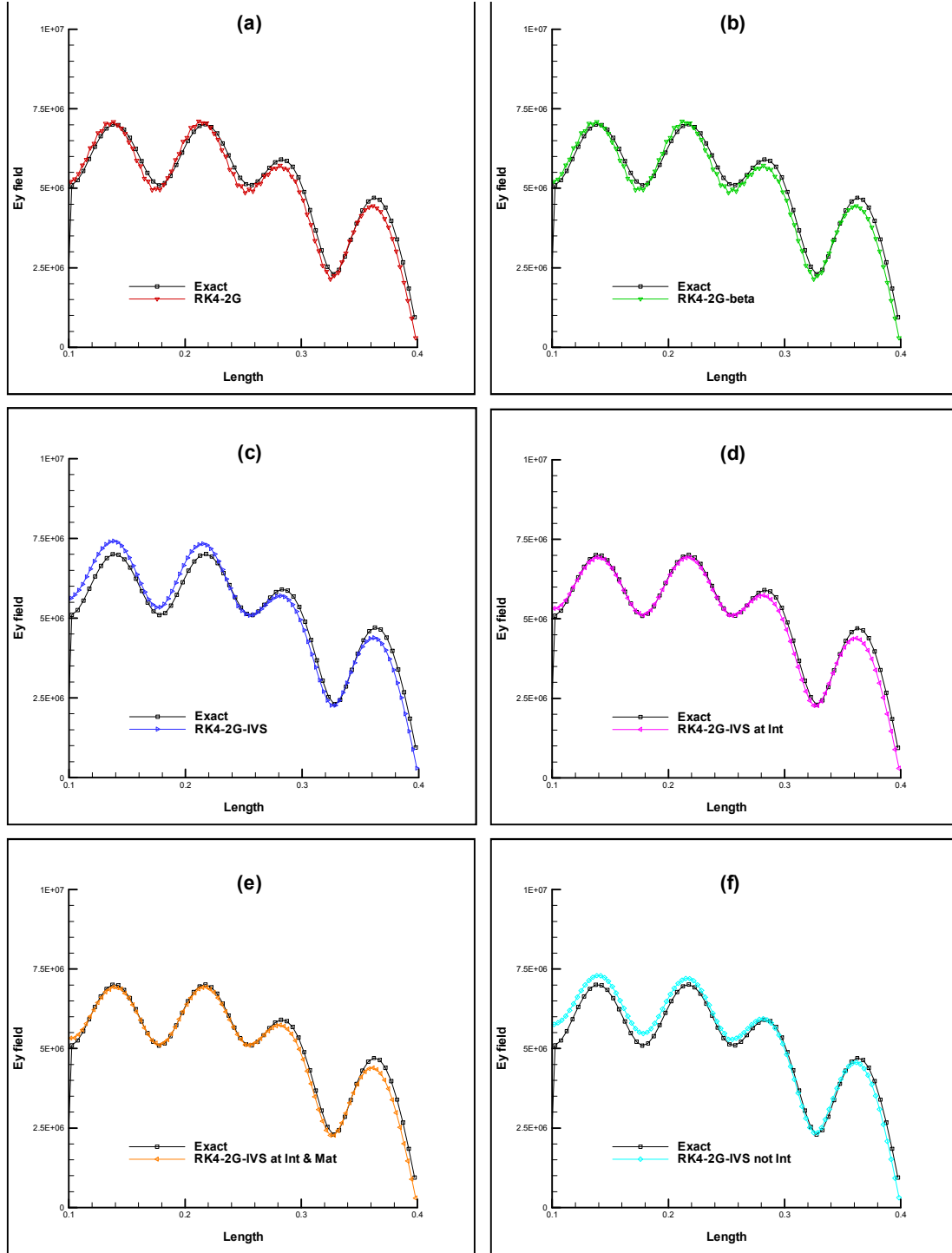
27

Figure 9. A fully loaded waveguide with $\varepsilon_r = 1 - 0.2j$; *(a) RK4-2G; (b) RK4-2G-beta;*

(c) RK4-2G-IVS; (d) RK4-2G-IVS at interface; (e) RK4-2G-IVS at interface and material;
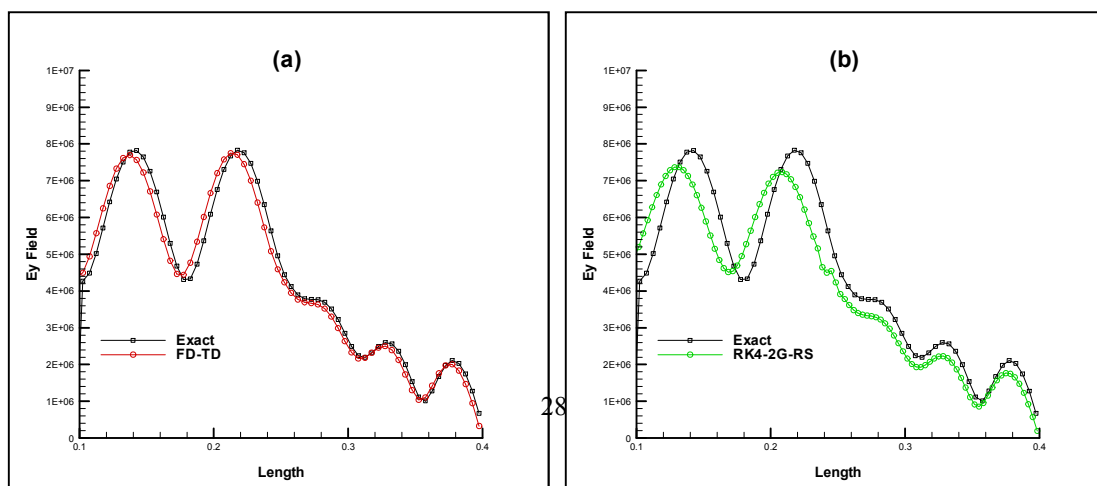
(f) RK4-2G-IVS not interface.

Figure 10. A fully loaded waveguide with $\varepsilon_r = 2 - 0.5j$; (a) FD-TD; (b) RK4-2G-RS; (c) SLF;

(d) SLF-beta; (e) RK3-2G; (f) RK3-2G-IVS.

By placing the unknowns $\mathbf{E}$ and $\mathbf{H}$ at the cell-centres, the schemes discussed in this paper evidently introduce oscillations in the numerical solutions, and these oscillations or errors cannot be completely removed without the inclusion of the damping effect in the discrete in space Maxwell's equations.
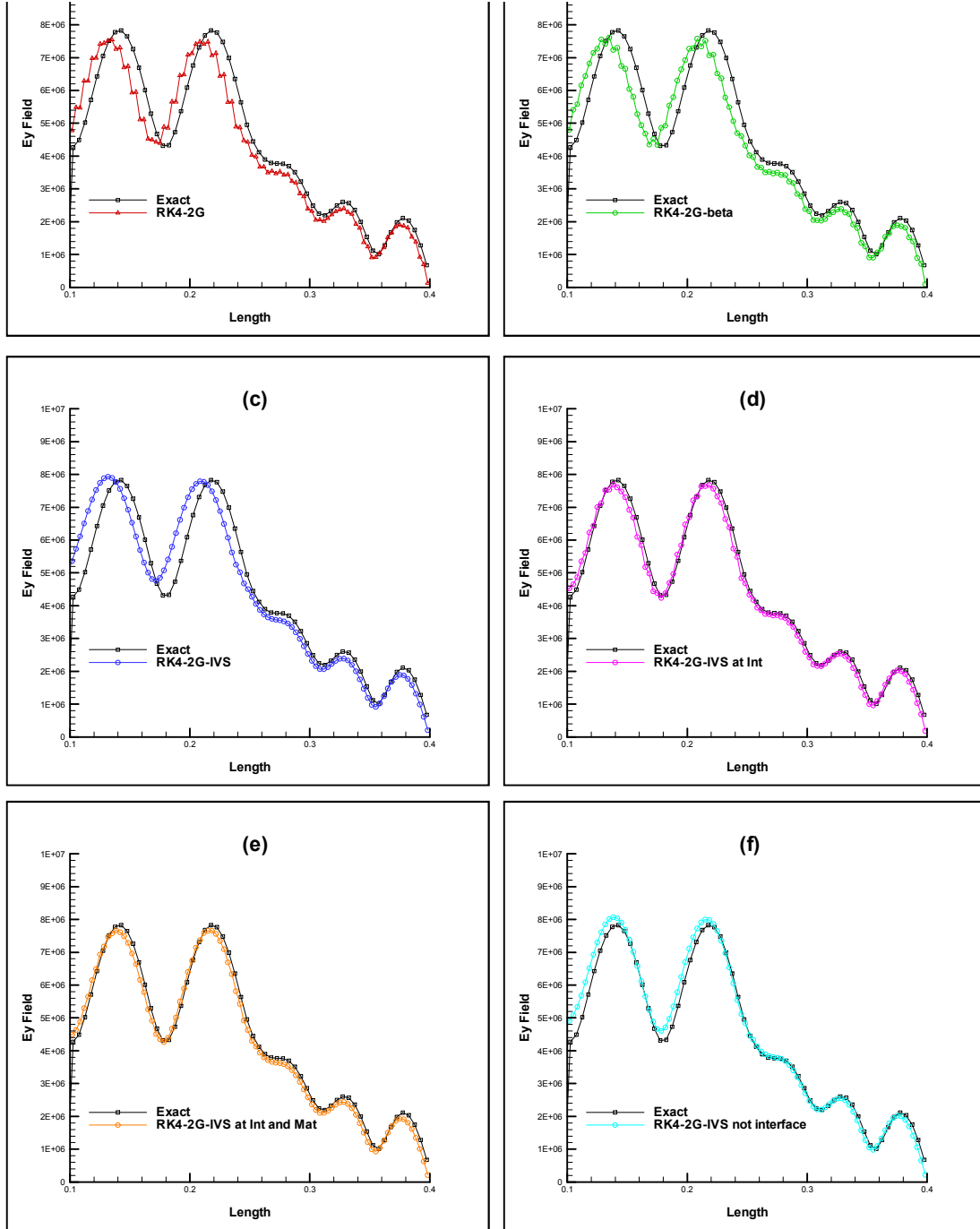
Figure 11. *A fully loaded waveguide with* $\varepsilon_r = 2 - 0.5j$; *(a) RK4-2G; (b) RK4-2G-beta;*

(c) RK4-2G-IVS; (d) RK4-2G-IVS at interface; (e) RK4-2G-IVS at interface and material;

(f) RK4-2G-IVS not interface.

By placing the unknowns $\mathbf{E}$ and $\mathbf{H}$ at the cell-centres, the schemes discussed in this paper evidently introduce oscillations in the numerical solutions, and these oscillations or errors cannot be completely removed without the inclusion of the damping effect in the discrete in space Maxwell's equations.

In Figs. (9c-f), the RK4 time integration with a number of applications of intensity vector splitting is established. It is clear from Figs. (9) and (11) that when IVS is used everywhere inside the computational domain there is damping in the solution.

Depending on the implementation of IVS (see Tab. (1)) within the numerical solver, the amount of reflection occurring at an interface can be subsequently affected. Figs. (11c-f) illustrate that by using the IVS result at a dielectric interface, the wave is better approximated. To reduce the loss of amplitude in the solution, the IVS result should only be used at an interface if there are gradient approximations present (14). Although, this is not to say that given higher order spatial discretisations, and hence higher order gradient approximations, the IVS schemes would not preform adequately everywhere. Higher order spatial discretisations will be the topic of future research.
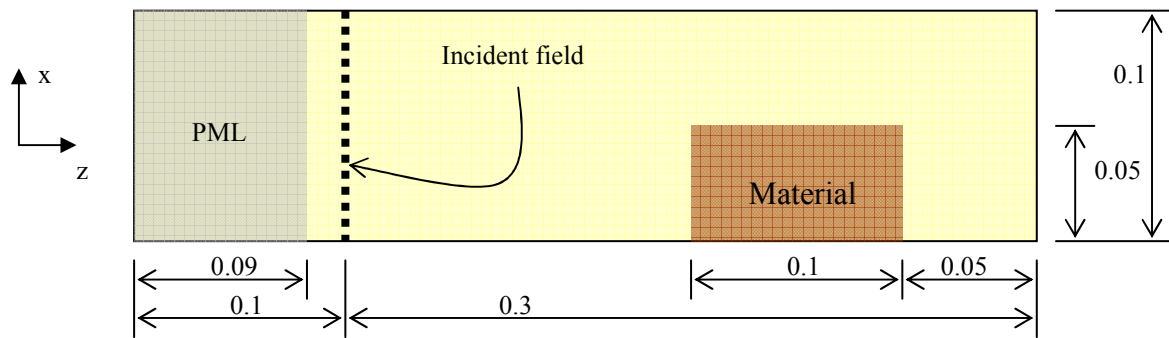
Figure 12. *The waveguide set up with dielectric of the multi-mode study.*

The studies conducted so far have all been on a single mode waveguide. The following sets of simulations were performed on the same waveguide with a load of permeability $\varepsilon_r = 2 - j$. The positioning of the load, incident field and PML absorbing layer is shown in Fig. (12). The simulations were run for sixteen periods, where the last two periods were averaged according to (31). The results shown are electric fields for the $y = 0.025$ plane. Fig. (13) exhibits the contour plots of the fields.

The material has height 0.05m, so that it completely fills the waveguide in the y-coordinate direction. Similarly to the previous examples, the domain has 96 000 (40 x 20 x 120) cells. The time stepping is chosen according to the restriction described in the first study.

It is clear in Fig. (13) that the introduction of damping removes the noise apparent in the other schemes that do not utilise IVS. FD-TD due to its staggered in space and time discretisation eliminates this error. The introduction of the beta correction tends to smooth the solution (see Figs. (13c-d)). For the SLF method with beta correction, the plane wave assumption was made on faces adjoining free space. From the Figs. (13c-d) there is an evident difference in the noise inside the guide. The effect of the beta correction slightly dampens the noise that is transmitted and reflected at a boundary. The methods that utilise IVS in Fig. (13) clearly approximate the solution in a smooth manner. Figs. (13e-f) demonstrate that the RK3-2G technique does not perform as well as the RK4-2G time integration procedure, whether with or without IVS. It can be concluded that RK3-2G methods have high loss of amplitude in waveguides where all the components of the fields exist. That is to say that when there is a load present, the lower order RK methods tend to have larger amplitude losses, even though they performed well in empty waveguide structures. When IVS was applied at the interface of free space and the material alone, the trends in the solution were very similar that to the RK4-2G solution (sees Fig. (13g)). The difference between the RK4-2G and the RK4-2G method that utilised IVS at an interface was the same as the difference between the SLF and SLF with beta correction techniques (see Figs. (13c-d)). Therefore, in waveguides that exhibit full field behaviour, the solution can be obtained to higher accuracy by applying some correction to the interface between free space and the dielectric. It should be noted that the FD-TD scheme demonstrated in Fig. (13a) also used the beta correction at the material interface. When simulating electromagnetic waves inside microwave heating apparatuses, special care should be taken for the treatment of the boundaries.
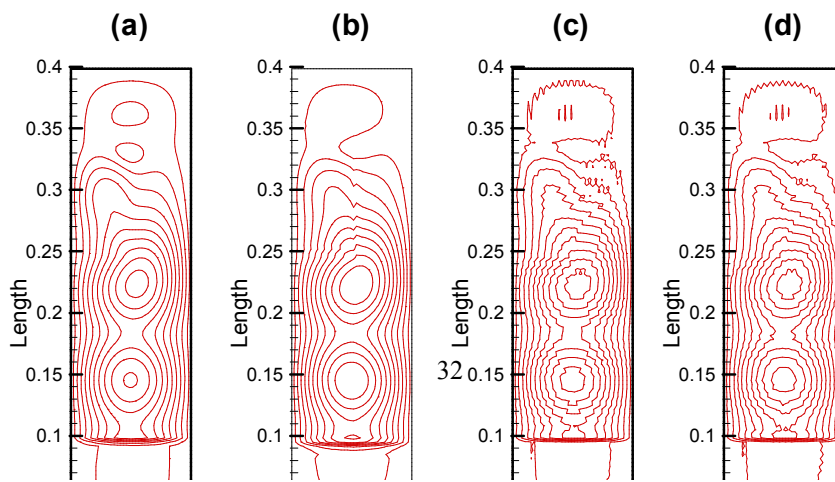

(a) (b) (c) (d)

32

Figure 13. Normalised 2D Contour plots of the electric field in a loaded multi-mode waveguide; (a) FD-TD;

(b) RK4-2G-IVS not interface; (c) SLF; (d) SLF-beta; (e) RK3-2G; (f) RK3-2G-IVS;

(g) RK4-2G; (h) RK4-2G-IVS.

In summary, from the previous case studies, the differences between the RK3 and RK4 time integration methods when applied to (4) were not obvious in Figs. (8-11). When this case study is analysed, it is evident that the higher the order of the numerical solver in time, the better it is able to capture the FD-TD solution (in terms of Runge-Kutta methods). Although the RK3 method requires less time than the RK4 method to approximate the solution, the solution obtained from the RK3 scheme may not be representative of reality. Although, it is possible to reduce the spatial mesh size to reduce errors in the RK3 methods, the cost of the extra computations on the larger number of grid cells outweighs the extra iteration in time required in approximating the next solution for the RK4 time stepping.

In conclusion, the results indicate that cell-centred schemes can be applied to capture the electromagnetic phenomena inside a waveguide. Methods such as ULF inherently incur large errors due to the discretisations, and therefore, are not recommended for real applications. The introduction of IVS, or the Riemann solver may dampen the fields, and special care should be taken when lower orders of spatial approximations are used. It was shown though that with special care and consideration, beta correction and IVS can be used in confidence to correct any oscillatory behaviour at material interfaces.

5. Conclusion

In this work, cell-centred finite-volume time-domain solvers for the Maxwell's equations were investigated and a number of solution strategies have been applied to resolve the different waveguide studies. It is well known that although the FD-TD method is very accurate, it is not straightforward to migrate it to unstructured domains. A number of cell-centred schemes have been formulated for structured domains, and further research in the area will demonstrate how these schemes can be implemented on completely unstructured grids.

An existing Petropolous type PML boundary region was investigated and the governing equations reformulated to enable it to be implemented in the new cell-centred solution methodology. It was shown that such an absorbing layer could be applied when simulating microwave heating problems using a cell-centred approach. The plane wave assumption around a material interface has been applied to schemes that do not utilise intensity vector splitting. Depending on the time integration technique and the properties of the material, the results were improved using this strategy. When intensity vector splitting or the Riemann solver was used, the results appeared to be smooth. This was due to the damping effect that these techniques induced in the numerical solution. Furthermore, it was shown that when using such techniques, care must be taken to insure that the solution is not overdamped, which could impose loss of significance in the solution. Special boundary treatments to cater for lower order dielectric interface conditions were formulated and demonstrated. Taking this into account, structured time-domain cell-centred numerical solvers for the solution of

Maxwell's equations in both an empty and loaded waveguide have produced reasonable results that were able to capture the time averaged electric fields sufficiently accurately. These time averaged electric fields are required to predict the power, and hence, the heating distribution inside a load within a waveguide.

This research demonstrates that for the purpose of microwave heating, cell-centred in space techniques can be applied to resolve the microwave power inside a dielectric material. Future research will analyse the techniques described here when applied on tetrahedral meshes both in a waveguide and a cavity structure.

6. References

1. Dibben, D.C. and A.C. Metaxas, *Time Domain Finite Element Analysis of Multimode Microwave Applicators Loaded with Low and High Loss Materials.* Intl. Conf. Microwave and High Energy Heating, 1995. **1-3.4**.

2. Zhao, H. and I. Turner, *An analysis of the finite-difference time-domain method for modelling the microwave heating of dielectric materals within a three-dimensional cavity system.* Journal of Microwave Power and Electromagnetic Energy, 1996. **31**(4): p. 199-214.

3. Madsen, N.K. and R.W. Ziolkowski, *A three-dimensional modified finite volume technique for Maxwell's equations.* Electromagnetics, 1990(10): p. 147-161.

4. Liu, Y., *Fourier Analysis of Numerical Algorithms for the Maxwell Equations.* Journal of Computational Physics, 1996. **124**: p. 396-416.

5. Yee, K.S., *Numerical Solution of Initial Boundary Value Problem Involving Maxwell's Equations in Isotropic Media.* IEEE Trans. Antennas Propagat., 1966. **14**: p. 302-307.

6. Shankar, V. and A.H. Mohammadian, *A Time-Domain, Finite-Volume Treatment for the Maxwell Equations.* 1990: p. 128-145.

7. Mohammadian, A.H., V. Shankar, and W.F. Hall, *Computation of electromagnetic scattering and radiation using a time-domain finite-volume discretization procedure.* Comp. Phys. Comm., 1991. **68**: p. 175-196.

8. Munz, C.D., R. Schneider, and U. VoB, *A finite-volume method for the maxwell equations in the time-domain.* SIAM Jouranl of Statistical Computing, 2000. **22**(2): p. 449-475.

9. Petropoulos, P.G., L. Zhao, and A.C. Cangellaris, *A Reflectionles Sponge Layer Absorbing Boundary Condition for the Solution of Maxwell's Equations with High-Order Staggered Finite Difference Schemes.* Journal of Computational Physics, 1998. **139**: p. 184-208.

10. Madsen, N.K. and R.W. Ziolkowski, *Numerical solution of Maxwells' equations in the time domain using irregular nonorthogonal grids.* Wave Motion, 1988(10): p. 583-596.

11. Taflove, A., *Re-inventing Electromagnetics: Supercomputing Solution of Maxwell's Equations Via Direct Time Integration on Space Grids.* AIAA paper 92-0333, 1992(New York).

12. Barth, T.J., *Aspects of Unstructured Grids and Finite-Volume Solvers for the Euler and Navier-Stokes Equations.* Lecture Notes Presented at the VKI Lecture Series, 1994-05, 1995.

13. Collin, R.E., *Field Theory of Guided Waves*. 1960: McGraw-Hill Book Company.

14. Mur, G., *Absorbing Boundary Conditions for the Finite-Difference Approximation of the Time-Domain Electromagnetic-Field Equations.* IEEE Trans. Microwave Theory Tech. EMC-23, 1981. **4**: p. 377-382.

15. Berenger, J.-P., *A Perfectly Matched Layer for the Absorption of Electromagnetic Waves.* Journal of Computational Physics, 1993. **114**: p. 185-200.

16. Berenger, J.-P., *Three-Dimensional Perfectly Matched Layer for the Absorption of Electromagnetic Waves.* Jounral of Computational Physics, 1996. **127**: p. 363-379.

17. Zhao, H., *Computational Models and Numerical Techniques for Solving Maxwell's Equations: A Study of Heating of Lossy Dielectric Materials Inside Arbitrary Shaped Cavities*, in *Centre in Statistical Science and Industrial Mathematics*. 1997, Queensland University of Technology: Brisbane.